

Evidence for Jet Collimation in SS 433 with the Chandra HETGS

Masaaki NAMIKI,^{1,2} Nobuyuki KAWAI,^{1,3} Taro KOTANI,^{3,4} and Kazuo MAKISHIMA^{1,5}

¹*The Institute of Physical and Chemical Research (RIKEN),
2-1, Hirosawa, Wako, Saitama. 351-0198*

²*Department of Physics, Tokyo University of Science,
1-3 Kagurazaka, Shinjuku-ku, Tokyo. 162-8601
namiki@crab.riken.go.jp*

³*Department of Physics, Tokyo Institute of Technology,
2-12-1, Ookayama, Meguro, Tokyo. 152-0033
nkawai@tithp1.hp.phys.titech.ac.jp*

⁴*Laboratory for High Energy Astrophysics, NASA Goddard Space Flight Center,
Greenbelt, MD, 20771, U.S.A.
kotani@milkyway.gsfc.nasa.gov*

⁵*Department of Physics, University of Tokyo,
7-3-1, Hongo, Bunkyo-ku, Tokyo. 113-0033
maxima@phys.s.u-tokyo.ac.jp*

(Received 2002 October 24; accepted 2002 November 19)

Abstract

High-resolution X-ray spectra of SS 433 obtained after a binary egress with the Chandra High Energy Transmission Grating Spectrometer (HETGS) were studied. Many Doppler-shifted X-ray emission lines from highly ionized elements were detected. The initial temperature of the jets is estimated to be 20 keV. The lines are found to generally be broader than the instrumented resolution. The widths of the Fe XXV $K\alpha$ and Si XIII $K\alpha$ lines correspond to velocity dispersions of 2100_{-340}^{+600} km s⁻¹ and 840_{-150}^{+180} km s⁻¹ respectively, in terms of Gaussian sigma. Neither the measured line widths nor their dependence on the atomic number can be explained by thermal broadening alone. Alternative explanations of the observed line widths are discussed, including in particular a progressive jet collimation along its axis.

Key words: Jets — Stars: individual (SS 433) — Stars: binaries: general — X-rays: individual (SS 433) — X-rays: spectra

1. Introduction

SS 433 is an enigmatic X-ray binary (orbital period ~ 13.1 d) with bipolar jets ejecting matter at a relativistic velocity of 0.26–times the light speed. The jet axis precesses with a period of ~ 162.5 d. Although SS 433 has been studied for more than 20 years since its discovery, its fundamental properties, such as the origin of the jet’s acceleration and precession, and the nature of the compact object, remain unknown.

The first intensive X-ray studies of SS 433 were performed by the Einstein Satellite. Then, SS 433 was revealed to be a variable X-ray source (Grindlay et al. 1984; Band, Grindlay 1986). Indeed, Watson et al. (1986) and Matsuoka et al. (1986) soon after found a Doppler-shifted FeXXV $K\alpha$ emission line in the X-ray spectra of SS 433 obtained by EXOSAT and the Tenma, respectively; they detected one emission line, and Watson et al. (1986) concluded that the X-ray emitting part of the receding jet is hidden behind the accretion disk. Thus, the length of the X-ray jet was estimated to be shorter than the orbital separation, $\lesssim 10^{12}$ cm. From the Ginga data, Kawai et al. (1989) determined the temperature of the jet to be 35 keV by modeling the continuum with thermal bremsstrahlung. Brinkmann et al. (1991) applied a hydrodynamical numerical model to the Ginga data, and estimated the initial temperature of the jet to be as high as ~ 40 – 70 keV. Since their solution implied a short ($\sim 10^{10}$ cm) jet with a high ($\sim 10^{13}$ cm $^{-3}$) density, the receding jet was considered to be easily hidden by the accretion disk, to become consistent with the EXOSAT data.

In 1993, however, a spectrum taken with ASCA, with its high-energy resolution and high sensitivity has overthrown the view so far established: the spectrum showed full “pairs” of Doppler-shifted emission lines from heavy elements such as Si XIV, S XV, S XVI, Ar XVII, Ar XVIII, Ca XIX, Fe XXV, Fe XXVI, and Ni XXVII (Kotani et al. 1994; Kawai 1995). Their detection implies that the approaching and receding jets are both visible, so that the X-ray jets are longer ($\sim 10^{13}$ cm) than previously estimated. Kotani et al. (1996) determined the base temperature of the jet to be 20 keV from the line flux ratio of Fe XXVI $K\alpha$ to Fe XXV $K\alpha$. Further analysis of the spectra revealed that the kinetic luminosity of SS 433 far exceeds the Eddington luminosity for any stellar size object (Kotani 1998). Kotani (1998) also suggested that the highly ionized iron $K\alpha$ lines are clearly seen in all of the data sets, while the low-energy emission lines from the receding jet are generally weaker than those from the approaching jet, and sometimes absent. This can be explained if absorbing matter is present in the line of sight to the receding jet.

Although the ASCA spectra thus revealed many emission lines which no previous mission was able to detect, the energy resolution of the ASCA SIS is still insufficient to fully resolve the emission line forest; this is particularly the case at energies below ~ 3 keV, where lines from different elements overlap and the effect of the absorption is severest. The Chandra High Energy Transmission Grating Spectrometer (HETGS) is ideal for an attempt to significantly

improve the knowledge obtained with ASCA. An important feature of the HETGS is that spectra are obtained independently and simultaneously using the High Energy Gratings (HEGs) and Medium Energy Gratings (MEGs). The HEGs have a twice-higher spectral resolution and a larger effective area above 4 keV than the MEGs, while the MEGs have an extended band-pass and a larger effective area for detecting low-energy emission lines. The energy resolution (FWHM) of the HEGs is $\sim 0.2\%$ at 2.0 keV and $\sim 0.5\%$ at 6.0 keV, while that of MEGs is $\sim 0.14\%$ at 0.8 keV and $\sim 0.33\%$ at 2.0 keV. Marshall et al. (2002) reported on the first observation of SS 433 using the Chandra/HETGS, made on 1999 September 23. The lines were measurably broadened to 1700 km s^{-1} (FWHM), and the widths did not depend significantly on the line-center energy, suggesting that the emission occurs in a freely expanding region of constant collimation with an opening angle of $1^\circ.26 \pm 0^\circ.06$. Furthermore, the excellent angular resolution of Chandra has revealed for the first time that the image of SS 433 is extended along the east-west direction on a scale of $2''\text{--}5''$, which is comparable to that observed in the radio band (Hjellming, Johnston 1981). These impressive results suggest that the Chandra X-ray Observatory will give us another surprise regarding this fascinating source.

2. Observations

The present observation of SS 433 was performed with the Chandra HETGS on 2001 May 12 UT10:38–16:33, which was on schedule with our proposal. The total exposure time was 19.7 ks. The corresponding orbital phase was 0.2832 ± 0.0094 (Gladyshev et al. 1987), when the compact object (including the two jets) and the accretion disk emerge out of an eclipse by the companion star. The Doppler-shift parameters at this observation were expected to be around $z_{\text{bl}} \sim +0.075$ and $z_{\text{rd}} \sim -0.004$ for the approaching and receding jets, respectively, according to the ephemeris of Margon and Anderson (1989). Usually, the jet directed to the east (called “blue jet”) is approaching us, and that to the west (“red jet”) is receding. However, the expected precessional phase on 2001 May 12 was reversed in such a way that the “blue jet” is receding and the “red jet” is approaching. This reversal occurs for a minor fraction ($\sim 50 \text{ d}$) of the 162.5 d precession period.

The observation log is shown in table 1. All the data were acquired in the ACIS-S faint mode with CCD chips S0, S1, S2, S3, S4 and S5, and processed in a standard way. The average flux of SS 433 in the 1–10 keV band was $8.7 \times 10^{-11} \text{ erg s}^{-1} \text{ cm}^{-2}$, corresponding to a luminosity of $2.4 \times 10^{35} \text{ erg s}^{-1}$, assuming a source distance of 4.85 kpc (Vermeulen et al. 1993). This luminosity is typical of SS 433.

3. Analysis and Results

3.1. Data Reduction

Figure 1 shows the zeroth-order image and the dispersion lines of SS 433 taken with the ACIS-CCD. Each of the “arms” of X pattern, formed by diffraction, yields the first-order spectrum specified by the grating type (HEG or MEG) and sign of the order (plus or minus). In the image, there are no obvious point sources, except for SS 433. On-source event counts have been accumulated on the dispersed image over narrow strips along the dispersion lines, of width $2''.39$ on either side. Background counts have been accumulated along similar strips, on both sides of each dispersion line, with a distance range of $2''.39$ – $23''.9$. The present study utilizes the dispersed data of $+1$ and -1 orders, by co-adding them together because no significant discrepancy is seen between them.

The spectral extraction and data reduction were all performed with the standard pipeline for the Chandra HETGS provided by the Chandra X-ray Center (CXO). The following data analysis utilizes the Chandra Interactive Analysis of Observations (CIAO) version 2.0 and custom routines in XSPEC. The spectra obtained by the HEG/HETGS in the total energy band are shown in figure 2.

When the energy-bin widths are chosen to be comparable to the energy resolution of the data, the statistics for each energy bin are so limited that the χ^2 minimization criterion is inappropriate for evaluating the spectral model fits. Instead, the fits are evaluated via minimum likelihood method, using the function

$$C = 2 \sum_{i=1}^N [y(x_i) - y_i + y_i(\ln y_i - \ln y(x_i))],$$

where x_i is the energy at the i -th bin, y_i is the observed data at x_i , and $y(x_i)$ is the value of the fitting function. Minimizing C gives the best-fit model parameters (Cash 1979; XSPEC User’s Guide for version 11.2.x, p.151). The C -statistic assumes that the errors on the counts are purely Poissonian, and hence it cannot deal with background-subtracted data. Therefore, the background is not subtracted in the following analysis. This is justified, because the background count rate is only 0.4% of the signal count rate, as is clear from figure 2.

The jet precession parameters of Margon and Anderson (1989) predict the Fe xxv $K\alpha$ lines from the blue and red jets to appear at energies of 6.236 and 6.718 keV, respectively. Indeed, the on-source spectrum exhibits a strong feature over an energy range of 6.3–6.8 keV (figure 2). In an expanded spectrum over this energy range, given in figure 3, the emission feature is resolved into a series of emission lines. However, none of them corresponds in energy to the predicted Fe xxv $K\alpha$ lines. This suggests that the jet-precession phase has deviated from the prediction. Actually, a series of optical spectroscopy of SS 433, performed at Gunma Astronomical Observatory (GAO) over a period spanning from 2001 May 12 (simultaneous with the present Chandra observation) to the end of 2001 November, consistently imply ~ 20 d phase

advance from the prediction (a private communication with K. Kinugasa and H. Kawakita; Namiki 2003 in preparation). Below, the jet redshifts are re-evaluated in reference to the optical data.

3.2. Spectral Fitting in the Hard Band

In figure 3, the HEG/HETGS spectrum in 5.5–8.5 keV energy band around the iron lines is fitted with a model consisting of a power-law continuum and narrow Gaussian lines. The fitting model is given, as a function of energy E , as

$$e^{-\sigma(E)N_{\text{H}}} \times \left[A \times E^{-\Gamma} + \text{Fe I K}\alpha_{z=0} + \text{Fe I K}\beta_{z=0} \right. \\ \left. + (\text{Fe XXV K}\alpha + \text{Fe XXVI K}\alpha + \text{Ni XXVII K}\alpha + \text{Fe XXV K}\beta)_{z=z_{\text{red}}} \right. \\ \left. + (\text{Fe XXV K}\alpha + \text{Fe XXVI K}\alpha + \text{Ni XXVII K}\alpha + \text{Fe XXV K}\beta)_{z=z_{\text{blue}}} \right], \quad (1)$$

where $\sigma(E)$ is the photo-electric cross-section at E , N_{H} is the equivalent hydrogen column density, while A and Γ are the normalization and photon index of the power-law continuum, respectively. The fitting model includes Gaussian components corresponding to ten emission lines, as specified by the line names in equation (1): four pairs of Doppler-shifted ionized lines (Fe XXV K α , Fe XXVI K α , Ni XXVII K α and Fe XXV K β) from the two jets, and two stationary lines (Fe I K α and Fe I K β). The rest-frame center energies of the lines were fixed to the theoretical values, while the overall Doppler shifts of the blue and red jets were set free; the redshift is common among all of the lines belonging to the same jet. The model is subjected to photoelectric absorption, with N_{H} fixed to the value which is determined in the lower energy band (subsection 3.3).

On the same May 12, the Doppler shifts in the optical band were obtained using H α lines at GAO as $+0.0424 \pm 0.0076$ and $+0.0204 \pm 0.0147$ for the blue and red jet, respectively. Considering the general agreement between the X-ray and optical Doppler shifts (within ≤ 0.64 d in the precessional phase; Kotani 1998), the optical redshifts were employed as initial values of the X-ray spectral fitting. As a result, the energies of Fe XXV K α lines were obtained at 6.410 and 6.524 keV ($z = 0.0449$ and 0.0267) for the blue and red jets, respectively, as given in table 2 and presented in figure 3. These values agree, within the respective errors, with the optical measurements at GAO. The observed precessional phase is such that the Fe XXV K α lines from the two jets and the fluorescent iron line from the accretion disk are heavily blended together around 6.5 keV. However, thanks to the excellent energy resolution of the HETGS, the lines were clearly resolved, except for an overlap between Fe I (6.399 keV) and Fe XXV K α of the blue jet (6.410 keV); these two lines, both known to be generally intense, could not be separated even with the energy resolution of the Chandra HETGS. However, this does not affect the determination of the jet redshifts, since the other lines contribute. Furthermore, as described later, the fluxes of the two overlapping lines can be determined separately with a sufficient accuracy by referring to their line widths.

The lower panel of figure 3 shows the ratio of the spectrum against the best-fit model described by equation (1), with the Gaussians all constrained to be narrow. There, large residuals are seen on both sides of each iron emission line. Thus, the lines are inferred to be broad, as already reported by Marshall et al. (2002) based on the same instrumentation. As shown in figure 4, a much better fit was obtained by allowing the Gaussians for the Doppler-shifted lines to have a common finite width; the C -statistics value decreased significantly from 851.94 (d.o.f. = 595) to 703.57 (d.o.f. = 594), and the residual between the fitting model and the data points disappeared. By using Monte Carlo methods to evaluate the absolute fit goodness, the narrow Gaussian model was completely rejected, while the broad Gaussian model was acceptable at a 2.7σ confidence interval. The Gaussians for the stationary fluorescent lines were kept narrow, because they are thought to come from a vicinity of the compact object. The width (standard deviation) of the Doppler-shifted lines has been constrained as $\sigma \sim 39.5^{+7.7}_{-6.5}$ eV, or 1850^{+360}_{-300} km s⁻¹ in terms of the Doppler velocity dispersion. Although the Fe xxv $K\alpha$ line is intrinsically broad due to the triplet structure (resonance, intercombination and forbidden), the Gaussian width decreases insignificantly to $35.9^{+7.9}_{-5.8}$ eV even considering the triplet. Here, the intensity ratio of the triplet lines was assumed to be 1.0 : 0.28 : 0.23 for the resonance, intercombination and forbidden lines, respectively, calculated by Mewe et al. (1985) at a plasma temperature of 20 keV.

The jet redshifts of SS 433 change continuously with time. Therefore, the line width may be caused by drifts in the redshifts during the observation. However, the total data span of the present observation, only 21.3 ks, is expected to cause changes in the iron line energies by no more than 4.0 eV, which is too small to explain the observed line width. For a further confirmation, the spectrum was divided into two parts, the former and latter half of the exposure time, and each data were fitted independently. In the case of Fe xxv $K\alpha$, the differences of the line center energy were obtained as 9.0 ± 29.4 eV and 30.0 ± 41.0 eV for the blue and red jet, respectively. As a result, no significant difference was found between the two spectra, and they both exhibited broad lines.

3.3. Spectral Fitting in the Soft Band

Figure 5 shows the spectra obtained by the MEG and HEG in the soft band (1.5–4.0 keV). Below, they are fitted jointly.

First, the data were fitted with a model of a power-law continuum and narrow Gaussian lines with photoelectric absorption, just in the same way as was performed in subsection 3.2, using the redshifts derived there as initial values. The fitting model is given as

$$\begin{aligned}
 & e^{-\sigma(E)N_{\text{H}}} \times \left[A \times E^{-\Gamma} \right. \\
 & + (\text{Si XIII } K\alpha + \text{Si XIV } K\alpha + \text{Si XIV } K\beta + \text{S XV } K\alpha + \text{S XVI } K\alpha)_{z=z_{\text{red}}} \\
 & \left. + (\text{Si XIII } K\alpha + \text{Si XIV } K\alpha + \text{Si XIV } K\beta + \text{S XV } K\alpha + \text{S XVI } K\alpha)_{z=z_{\text{blue}}} \right], \tag{2}
 \end{aligned}$$

where the helium-like emission lines include the resonance and forbidden components, and the other annotations of this model are the same as those in subsection 3.2. As a result, a clear local minimum in the fit C -statistics has been obtained at $z_{\text{bl}} = 0.0446$ and $z_{\text{rd}} = 0.0220$, both close to the input initial values. As shown in figure 5, this fit implies the presence of Si XIII $K\alpha$, Si XIV $K\alpha$, S XV $K\alpha$, and S XVI $K\alpha$ lines from the two jet components.

Although the spectra were thus represented approximately by equation (2), significant fit residuals are again observed on both sides of each line. As shown in figure 6, the fit was greatly improved by allowing the lines to have a finite common width; the C -statistics value has decreased from 1508.82 (d.o.f. = 1236) to 1468.32 (d.o.f. = 1235). The Monte Carlo calculation indicates that the former is completely rejected, while the latter is acceptable at a 5.0 σ confidence interval. The model parameters were obtained as given in table 3. The redshift of the blue jet is consistent within the 90% statistical error with that obtained in the hard band (table 2). Although the redshift of the red jet is inconsistent with that in the hard band, it can be understood by considering the systematic errors (± 0.006 Å for HEG; ± 0.011 Å for MEG). The Gaussian width (standard deviation) was obtained to be $\sigma = 5.2^{+1.1}_{-0.9}$ eV, or 870^{+190}_{-150} km s⁻¹ in terms of the Doppler velocity dispersion.

Even in the broad-line fit in figure 6, there still remain residuals around 1.85 keV, approximately exhibiting a double-peaked feature. This feature was successfully modeled by two Gaussians with central energies at 1.847 and 1.874 keV and a finite width of $\sigma = 6.8^{+1.6}_{-1.2}$ eV. Adding these two lines made the goodness-of-fit of the present model satisfactory at a 1.0 σ confidence interval. However, taking the obtained Doppler shifts into account, the energies of these two additional lines do not correspond to the atomic lines of any major element, and hence they cannot be represented by the jet components.

3.4. Spectral Fitting over the Total Band

By analyzing the HETGS spectra in the Fe $K\alpha$ and Si $K\alpha$ bands separately, it has been suggested that a common set of z_{bl} and z_{rd} can reproduce the overall data, but the Fe $K\alpha$ lines are more broadened (in terms of the Doppler velocity dispersion) than the Si $K\alpha$ lines. In order to confirm these two inferences, it is appropriate to fit the two spectral regions simultaneously.

The data were thus fitted over the total (1.5–9.0 keV) energy band with a model which combines those presented in equation (1) and equation (2). The photoelectric absorption, the photon index and intensity of the power-law, and the jet redshifts were constrained to be common between the two energy bands, while the line widths were allowed to take separate values in the hard and soft bands. The unidentified features (at 1.847 and 1.874 keV) were left unmodeled in order to reduce the number of free parameters. The results of subsection 3.2 and 3.3 were used for the initial parameters in the respective energy bands. The joint fit has been acceptable (at 5.0 σ), and the jet redshifts, line intensities, and the line widths turned out to be consistent with those from the individual fits. Although the power-law parameters and the

absorption column density slightly disagree with those obtained in the limited energy bands, this is a relatively minor effect (table 4).

The most important information obtained from this fit is the relation between the widths of low-energy and high-energy lines. As presented in figure 7, the results clearly confirm that the velocity dispersion of the high energy lines is significantly larger than that of the low-energy lines.

4. Discussion

4.1. Jet Temperature

The intensity ratios among emission lines provide important information on the physical conditions of cosmic hot plasmas. In particular, the intensity ratio of the $K\alpha$ line from Fe XXVI to that of Fe XXV provides a clear temperature indicator for very hot plasmas, and hence can be used to constrain the jet parameters of SS 433. By comparing the ASCA measurements with detailed model calculations, Kotani et al. (1996) estimated the typical initial temperature of the jets to be $T_0 \sim 20$ keV. In the present observation, the intensity ratio of the $K\alpha$ line from Fe XXVI to that of Fe XXV was obtained as 0.46 ± 0.17 and 0.42 ± 0.17 , for the blue and red jet, respectively, which translate to $T_0 = 19.5^{+8.8}_{-6.9}$ and $T_0 = 17.2^{+8.0}_{-6.7}$ keV according to the model of Kotani et al. (1996). From these values, the jet activity of SS 433 is inferred to have been in a normal state during the observation.

In contrast, Marshall et al. (2002) derived significantly lower values of T_0 , based on the Chandra HETGS observation on 1999 September 23 (orbital phase ~ 0.67). In the spectra of Marshall et al. (2002), the Fe XXVI lines from the jets were so weak that the intensity ratios of the iron lines were 0.30 ± 0.12 and 0.17 ± 0.08 for the blue and red jets, respectively, yielding $T_0 = 12.9^{+4.7}_{-4.3}$ and $T_0 = 8.6^{+2.4}_{-2.1}$ keV. Because these temperatures are lower than the usually reported values (~ 20 keV), it appears that the high-energy lines, emitted near the base of the jet of SS 433, were at that time hidden by something, such as an expanded accretion disk. Thus, it is likely that Marshall et al. (2002) observed an unusual low-activity state of SS 433. The present paper provides the first report on the high-resolution X-ray spectroscopy of SS 433 in a relatively normal state, which is close to the past usual states observed with Ginga and ASCA.

4.2. Line Widths

The Doppler-shifted lines of SS 433, measured with the HETGS, have been successfully represented by broad Gaussian models. The obtained line widths are $\sigma = 44.5^{+12.9}_{-7.3}$ eV and $\sigma = 5.0^{+1.1}_{-0.9}$ eV, or $v_{\text{Fe}} = 2100^{+600}_{-340}$ km s⁻¹ and $v_{\text{Si}} = 840^{+180}_{-150}$ km s⁻¹ in terms of the Doppler velocity dispersion, for the high-energy (mainly iron) and low-energy (mainly silicon) lines, respectively. Marshall et al. (2002) also measured finite widths from the Doppler-shifted lines, although the widths were not much different from element to element. Figure 8 summarizes the velocity

dispersion of various $K\alpha$ lines, from the present work and Marshall et al. (2002), as a function of the atomic number. Thus, the two measurements agree very well on the low-energy lines, while not on the high-energy lines. This may be caused by the low activity of SS 433 during the observation by Marshall et al. (2002), as suggested by the low values of T_0 . If the high-energy elements, above calcium, of Marshall et al. (2002) are excluded, figure 8 reveals a clear positive dependence of the velocity dispersion on the atomic number.

In figure 8, the dashed curves represent the velocity dispersion expected when the line widths are caused solely by thermal broadening, for several representative ion kinetic temperatures. Thus, the measured line widths are too large to be explained in terms of thermal Doppler effect, for a reasonable range of temperature where the atomic emission lines are significantly emitted. Furthermore, the measured positive correlation of the velocity dispersion on the atomic number is opposite to what is predicted by the thermal Doppler effect. For these reasons, the thermal broadening is concluded to be inappropriate as an account of the measured line widths.

The Compton scattering is another candidate of generating the line widths. The X-rays lines may be narrow when produced in the jets, and then Compton scattered in a surrounding medium to get broadened. This may work, because the optical depth of the jets to the electron scattering is of the order of unity (Kotani 1998). In this case, a single Compton scattering in a medium of electron temperature T_e is expected to shift the X-ray line energy E by $\Delta E \sim E(4kT_e - E)/m_e c^2$, where $m_e c^2$ is the electron rest-frame energy. Then, the measured values of $\Delta E \sim 5$ eV for silicon ($E \sim 1.8$ keV) and $\Delta E \sim 45$ eV for iron ($E \sim 6.7$ keV) require $T_e \simeq 0.8$ keV and 2.5 keV, respectively. The discrepant values of T_e may be explained by a picture that the high-energy lines are produced in a region closer to the central engine. However, such a scattering medium, having the necessary Compton optical depth (~ 1) and the inferred low T_e , would inevitably produce prominent edges from partially ionized atoms, which are not seen in the spectra. Therefore, Compton scattering may not be appropriate, either.

Another possible origin of the line widths and its dependence on the atomic number is a progressive collimation of the conical opening angle of the jets. Marshall et al. (2002) ascribed the line widths to the Doppler broadening that may result from the conical jet outflow, and concluded that the emission occurs in a freely expanding region of constant collimation with an opening half-cone angle of $\Theta = 1^\circ.23$; the opening angle produces a transverse velocity of the jet, which causes the obtained widths. Assuming an oppositely directed pair of jets observed at an angle α to the line of sight, the Doppler shifts of the blue and red jets are given by

$$1 + z = \gamma\{1 \pm \beta \cos(\alpha)\},$$

where β is the velocity of the jet in unit of c , and $\gamma = (1 - \beta^2)^{-1/2}$. Solving this equation for γ as

$$v_{\text{jet}} = \beta \times c = \left\{ 1 - \frac{1}{(1 + z_{\text{av}})^2} \right\}^{1/2} \times c,$$

where $z_{\text{av}} = (z_{\text{bl}} + z_{\text{rd}})/2$, and utilizing the observed redshifts, $v_{\text{jet}} = 0.2629 c$ and $\alpha = 92^\circ.1$ are obtained. The velocities of the perpendicular component against the direction of jet traveling are obtained as $v'_{\text{Fe}} = v_{\text{Fe}} \sin(\alpha) = 2100 \text{ km s}^{-1}$ and $v'_{\text{Si}} = v_{\text{Si}} \sin(\alpha) = 840 \text{ km s}^{-1}$. The velocity dispersion can be equated directly with $f v_{\text{jet}} \tan(\Theta)$, where f is a form factor depending on the emissivity distribution across the jet cross section. Assuming that the density is uniform through the cone's cross section and that the component of the velocity which is parallel to the jet axis is the same for all fluid elements in the slice, then a simple calculation gives $f = 0.74$ (Marshall et al. 2002). Therefore, the present observation yields

$$\Theta_{\text{Fe}} = \tan^{-1} \left(\frac{1}{f} \frac{v'_{\text{Fe}}}{v_{\text{jet}}} \right) = 2^\circ.1^{+0^\circ.6}_{-0^\circ.3},$$

$$\Theta_{\text{Si}} = \tan^{-1} \left(\frac{1}{f} \frac{v'_{\text{Si}}}{v_{\text{jet}}} \right) = 0^\circ.8 \pm 0^\circ.2.$$

Since the Fe-K lines are thought to be produced close to the central engine while the Si-K lines to come from those positions of the jets which are $\geq 10^{12}$ cm away from the center (Kotani 1998), the present results imply that the jet collimation is achieved over a distance of $\geq 10^{12}$ cm, or $\geq 10^2$ sec. This interpretation, if correct, provides valuable information as to the jet collimation mechanism.

Since the collimation is thus inferred to occur on a scale much larger than the accretion disk, it is more likely to be achieved by magnetic fields, rather than by any funnel-shaped structure in the accretion disk.

4.3. Unidentified Features

As mentioned in the last paragraph of subsection 3.3, the double-peaked features, which can be explained by neither the jet components nor the fluorescent lines from the accretion disk, were found around 1.86 keV. This energy corresponds to that of “stationary” Si XIII $K\alpha$ line. From a careful look at the spectra in figure 6, similar features are also suggested around 2.01 keV, 2.46 keV and 2.62 keV, tentatively identified with Si XIV $K\alpha$, S XV $K\alpha$, and S XVI $K\alpha$ lines. These unidentified features have not been detected for any other observation of SS 433 using the Chandra HETGS, and their exact nature remains unknown.

5. Summary

The analysis of the Chandra HETGS data of SS 433 acquired on the 2001 May 12 have yielded the following results:

1. The observed precessional phase of the jets was shifted by ~ 20 d from the prediction based on Margon and Anderson (1989).

2. The initial temperature of the blue and red jets are estimated to be $19.5_{-9.5}^{+7.8}$ and $17.2_{-6.8}^{+9.0}$ keV, respectively.
3. The Doppler-shifted lines were found to be broad, and the corresponding velocity dispersions are 2100_{-340}^{+600} km s⁻¹ and 840_{-150}^{+180} km s⁻¹ for the high-energy and low-energy lines, respectively.
4. While the observed line widths cannot be explained satisfactorily by the thermal Doppler effect or the Compton scattering, a successful explanation may be obtained by assuming that the line widths originate from the jet opening angle, and that the angle becomes narrower as the jets travel away from the central engine.

M. N. is supported by the Junior Research Associate Program of RIKEN. M. N. also would like to thank Dr. H. Matsumoto, Dr. H. L. Marshall, and the members of Center for Space Research (MIT) for the study of the Chandra HETGS. We thank the GAO for the good optical data and the meaningful discussion and suggestion.

References

- Band, D. L., & Grindlay, J. E. 1984, *ApJ*, 285, 702
- Brinkmann, W., Kawai, N., Matsuoka, M., & Fink, H. H. 1991, *A&A*, 241, 112
- Cash, W. 1979, *ApJ*, 228, 939
- Gladyshev, S. A., Goranskii, V. P., & Cherepashchuk, A. M. 1987, *Sov. Astron.*, 31, 541
- Grindlay, J. E., Band, D., Seward, F., Leahy, D., Weisskopf, M. C., & Marshall, F. E. 1984, *ApJ*, 277, 286
- Hjellming, R., & Johnston, S. 1981, *ApJ*, 246, L141
- Kawai, N., Matsuoka, M., Pan, H. C., & Stewart, G. C. 1989, *PASJ*, 41, 491
- Kawai, N. 1995, in 17th Texas Symp. on Relativistic Astrophysics and Cosmology, ed. H. Boehringer, G.E. Morfill, J.E. Trümper (New York: New York Academy of Science), 316
- Kotani, T., Kawai, N., Aoki, T., Doty, J., Matsuoka, M., Mitsuda, K., Nagase, F., Ricker, G., & White, N. E. 1994, *PASJ*, 46, L147
- Kotani, T., Kawai, N., Matsuoka, M., & Brinkman, W. 1996, *PASJ*, 48, 619
- Kotani, T. 1998, PhD Thesis, University of Tokyo
- Margon, B., & Anderson, S. F. 1989, *ApJ*, 347, 448
- Marshall, H. L., Canizares, C. R., Schulz, N. S. 2002, *ApJ*, 564, 941
- Matsuoka, M., Takano, S., & Makishima, K. 1986, *MNRAS*, 222, 605
- Mewe, R., Gronenschild, E. H. B. M., & van den Oord, G. H. J. 1985, *A&AS*, 62, 197
- Vermeulen, R. C., Schilizzi, R. T., Spencer, R. E., Romney, J. D., & Fejes, I. 1993, *A&A*, 270, 177
- Watson, M. G., Stewart, G. C., Brinkmann, W., & King, A. R. 1986, *MNRAS*, 222, 261

Table 1. Observation log.

Start time (UT)	End time (UT)	Orbital phase*	Exposure time
2001/05/12 10:38	2001/05/12 16:33	0.2832 ± 0.0094	19.7 ks

* Calculated from the parameters given by Gladyshev et al. (1987).

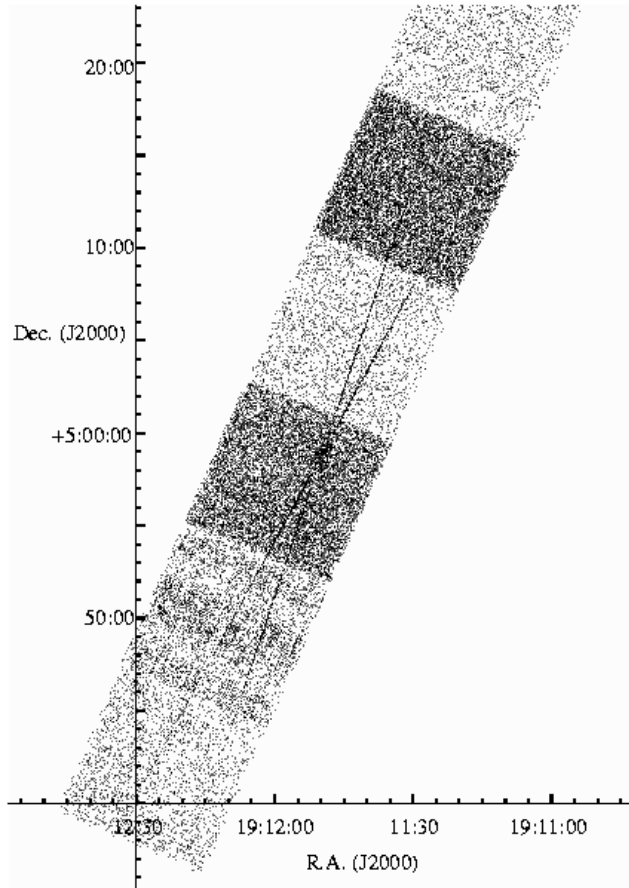


Fig. 1. Zeroth-order image and dispersion lines of SS 433 taken with the ACIS-CCD on 2001 May 12. The central point source (SS 433) and 4 lines (grating spectra) are shown in J2000 coordinates.

Table 2. Results of the model fit to the HETGS/HEG spectrum of SS 433 in the 4.0–9.0 keV band.*

Parameter	Blue	Red
Redshift	0.0460 ± 0.0013	0.0265 ± 0.0014
Line fluxes [†]		
Fe XXV K α (6.70)	$38.5^{+7.4}_{-6.5}$	$34.5^{+6.4}_{-6.1}$
Fe XXVI K α (6.97)	$17.6^{+5.5}_{-5.0}$	$14.3^{+5.2}_{-4.7}$
Ni XXVII K α (7.80)	$9.2^{+6.3}_{-5.3}$	< 5.1
Fe XXV K β (7.90)	$5.3^{+6.2}_{-5.0}$	$4.7^{+6.1}_{-4.7}$
Fe I K α (6.40)		$6.4^{+5.2}_{-4.8}$
Fe I K β (7.06)		$3.8^{+3.3}_{-2.6}$
Line width [‡]	$39.5^{+7.7}_{-6.5}$ eV	
Power law Γ	1.61 ± 0.07	
Power law A	$(1.63 \pm 0.03) \times 10^{-2}$ ph s ⁻¹ cm ⁻²	
N_{H}^{\S}	1.09×10^{22} cm ⁻² (fixed)	
C -statistic	703.57 (d.o.f. = 594)	

* All uncertainties refer to statistical 90% confidence limits.

In the case of redshift, a systematic error of ± 0.0033 must be added.

[†] The measured line fluxes, in unit of 10^{-5} ph s⁻¹ cm⁻². The number in parenthesis shows the rest-frame line energy, in unit of keV.

[‡] Common to all the ion species.

[§] Column density of photoelectric absorption, determined in the soft energy band.

Table 3. Results of the model fit to the HETGS / HEG + MEG spectra of SS 433 in the 1.5–4.0 keV band.*

Parameter	Blue	Red
Redshift	0.0444 ± 0.0007	0.0220 ± 0.0008
Line fluxes [†]		
Si XIII f $K\alpha$ [‡] (1.85)	$1.0^{+1.2}_{-1.0}$	< 0.9
Si XIII $K\alpha$ (1.86)	$2.7^{+1.3}_{-1.2}$	$4.2^{+1.3}_{-1.3}$
Si XIV $K\alpha$ (2.01)	$7.3^{+1.6}_{-1.5}$	$5.4^{+1.5}_{-1.4}$
Si XIV $K\beta$ (2.38)	$3.0^{+2.4}_{-2.1}$	< 1.7
S XV f $K\alpha$ [‡] (2.45)	$1.9^{+2.4}_{-1.9}$	< 1.7
S XV $K\alpha$ (2.46)	$3.2^{+2.3}_{-2.0}$	$2.9^{+2.2}_{-2.0}$
S XVI $K\alpha$ (2.62)	$4.4^{+2.1}_{-1.9}$	$2.3^{+2.0}_{-1.7}$
Line width [‡]	$5.2^{+1.1}_{-0.9}$ eV	
Power law Γ	1.21 ± 0.05	
Power law A	$(9.41 \pm 0.07) \times 10^{-3}$ ph s ⁻¹ cm ⁻²	
N_{H}	$(1.09 \pm 0.07) \times 10^{22}$ cm ⁻²	
C -statistic	1468.32 (d.o.f. = 1235)	

* All uncertainties refer to statistical 90% confidence limits.

In the case of redshift, a systematic error of ± 0.0017 must be added.

[‡] Forbidden lines.

The other annotation symbols are the same as in table 2.

Table 4. Results of the model fit to the HETGS / HEG + MEG spectra of SS 433 in the 1.5–9.0 keV band.*

Parameter	Blue	Red
Redshift	0.0443 ± 0.0006	0.0227 ± 0.0007
Line fluxes [†]		
Si XIII f $K\alpha$ \parallel (1.85)	$1.0^{+1.3}_{-1.0}$	< 0.8
Si XIII $K\alpha$ (1.86)	$2.9^{+1.4}_{-1.4}$	$4.3^{+1.5}_{-1.4}$
Si XIV $K\alpha$ (2.01)	$7.8^{+1.8}_{-1.8}$	$5.8^{+1.6}_{-1.5}$
Si XIV $K\beta$ (2.38)	$3.0^{+2.5}_{-2.2}$	< 1.5
S XV f $K\alpha$ \parallel (2.45)	$2.0^{+2.4}_{-2.0}$	< 1.5
S XV $K\alpha$ (2.46)	$3.1^{+2.4}_{-2.1}$	$2.8^{+2.3}_{-2.0}$
S XVI $K\alpha$ (2.62)	$4.5^{+2.2}_{-2.0}$	$2.4^{+2.1}_{-1.8}$
Line width [#]	$5.0^{+1.1}_{-0.9}$ eV	
Fe XXV $K\alpha$ (6.70)	$42.6^{+7.3}_{-6.9}$	$30.9^{+6.6}_{-6.1}$
Fe XXVI $K\alpha$ (6.97)	$16.9^{+5.8}_{-5.2}$	$10.9^{+5.2}_{-4.6}$
Ni XXVII $K\alpha$ (7.80)	$9.6^{+6.7}_{-5.6}$	< 5.9
Fe XXV $K\beta$ (7.90)	$3.4^{+6.3}_{-3.4}$	$3.1^{+6.3}_{-3.1}$
Fe I $K\alpha$ (6.40)	$6.8^{+4.9}_{-4.5}$	
Fe I $K\beta$ (7.06)	$3.4^{+3.3}_{-2.6}$	
Line Width ^{**}	$44.5^{+12.9}_{-7.3}$ eV	
Power law Γ	1.40 ± 0.04	
Power law A	$(1.18 \pm 0.07) \times 10^{-2}$ ph s ⁻¹ cm ⁻²	
N_{H}	$(1.31 \pm 0.06) \times 10^{22}$ cm ⁻²	
C -statistic	2311.75 (d.o.f. = 1964)	

* All uncertainties refer to statistical 90% confidence limits.

In the case of redshift, a systematic error of ± 0.0017 must be added.

[#] The width for low-energy lines.

^{**} The width for high-energy lines.

The other annotation symbols are the same as table 2.

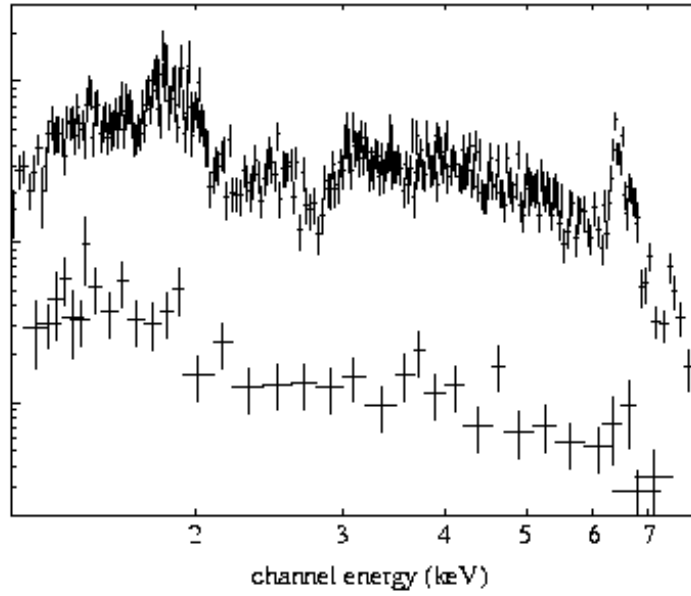


Fig. 2. Chandra HETGS spectra of SS 433 acquired on 2001 May 12, shown for the total (1.0–8.0 keV) band. The upper and lower spectra correspond to the source and background, respectively.

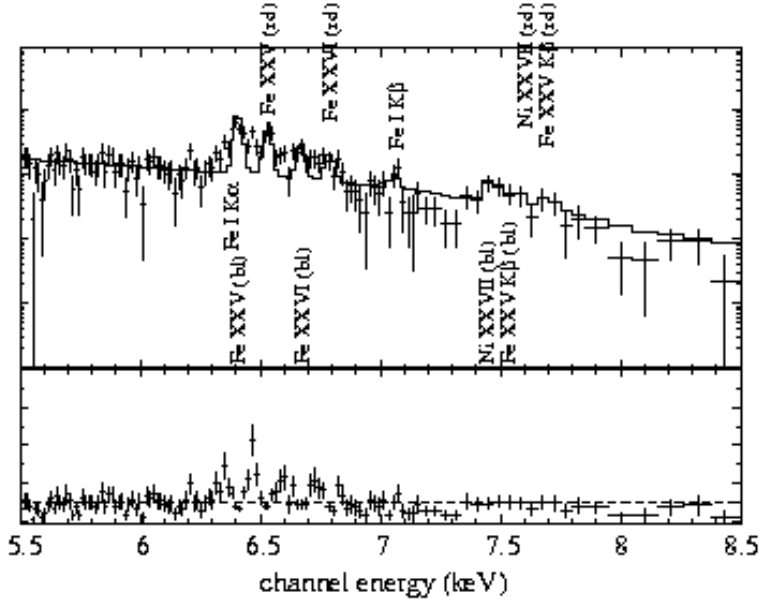


Fig. 3. Same on-source spectrum as presented in figure 2, shown over the iron K-line energy band. The solid histograms represent the best-fit jet emission model, in which the jet redshifts are left free but the lines are constrained to be narrow. The location of emission lines are labeled with ion species and the jet ID; “bl” denotes lines from the “blue jet”, and “rd” denotes those from the “red jet”. The bottom panel shows the intensity ratio against the best-fit model.

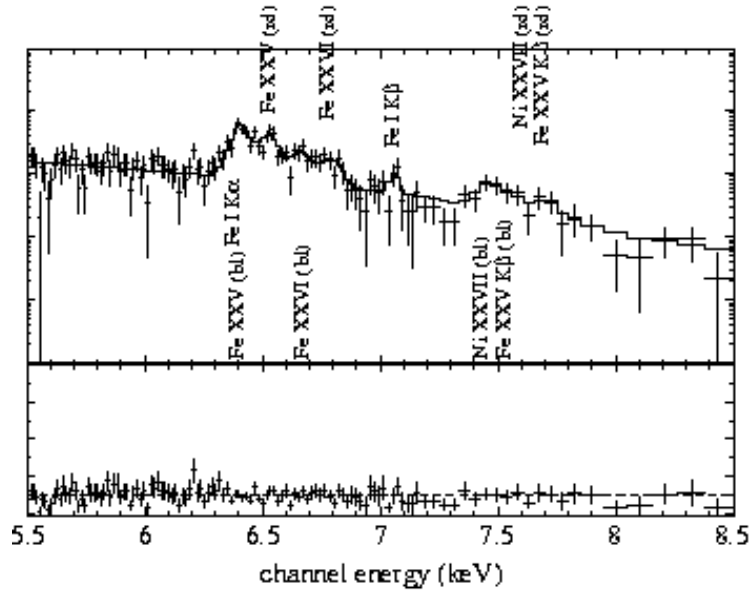


Fig. 4. Same as figure 3 , but the Doppler-shifted emission lines in the model are allowed to have a common width.

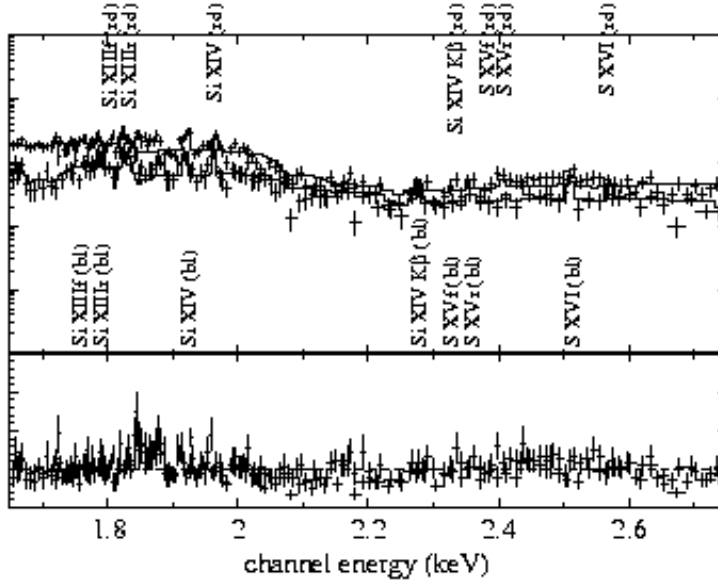


Fig. 5. Chandra HEG (lower) and MEG (upper) spectra of SS 433 taken on 2001 May 12, shown over the silicon K-line energy band. The subscripts “r” and “f” are for the resonance and forbidden components, respectively. The Gaussian lines are constrained to be narrow. The bottom panel shows the ratio against the best-fit model.

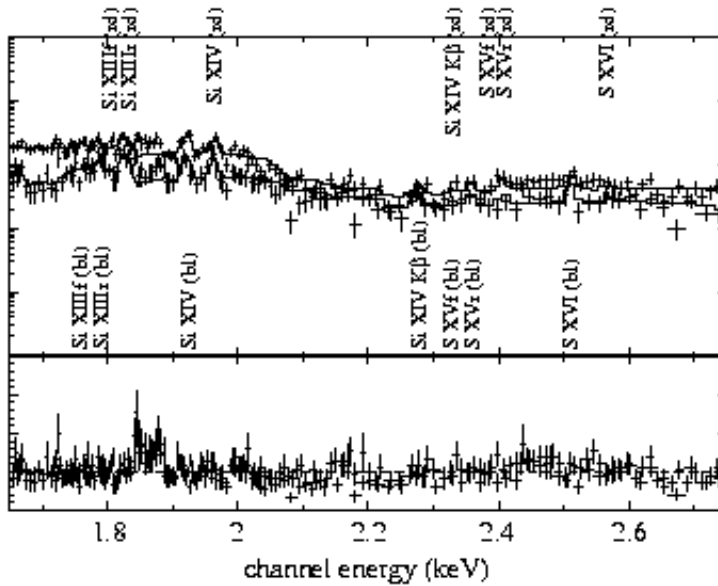


Fig. 6. Same as figure 5, but the emission lines in the model are allowed to have a common width.

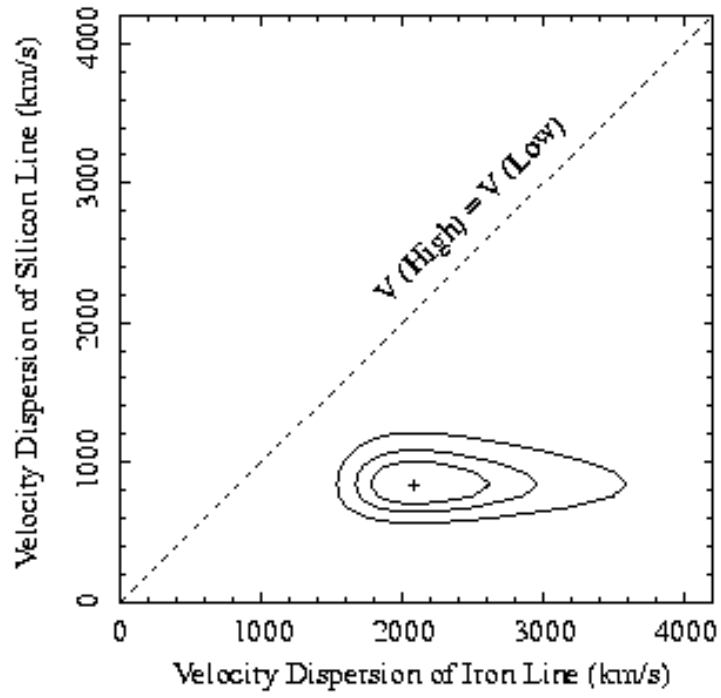


Fig. 7. Confidence contours for the velocity dispersion of Fe XXV $K\alpha$ and Si XIII $K\alpha$ lines. The contours correspond to the 99%, 90% and 68% confidence levels from outside to inside.

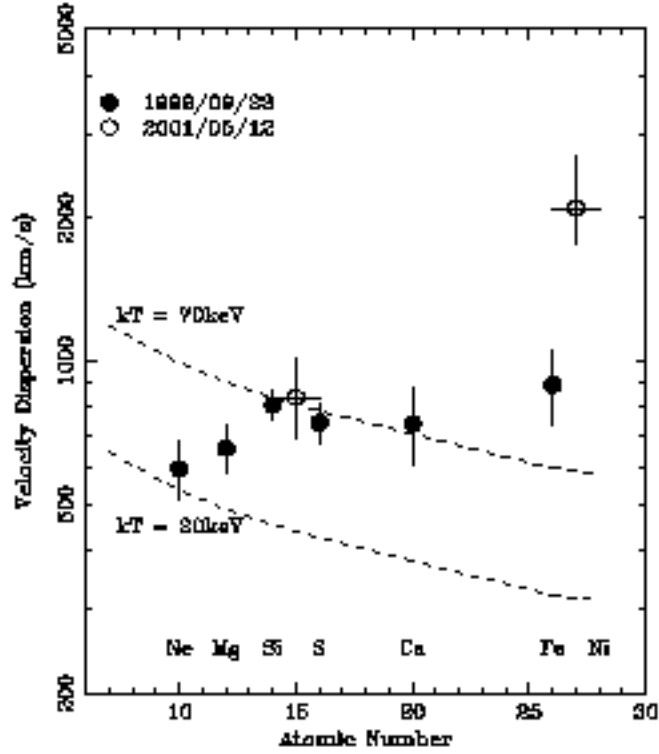


Fig. 8. Atomic number of $K\alpha$ line vs. its velocity dispersion. The filled and open circles correspond to the Chandra HETGS data observed on 1999 September 23 (Marshall et al. 2002) and 2001 May 12 (the present work), respectively. The dashed lines are velocity dispersions of the $K\alpha$ lines expected for thermal Doppler broadening. The upper one is for an ion kinetic temperature of 70 keV, and lower is for 20 keV.